Research Article | Vol. 12, No. 6 / 1 June 2021 / Biomedical Optics Express 3438
Biomedical Optics EXPRESS

# Non-contact terahertz spectroscopic measurement of the intraocular pressure through corneal hydration mapping

ANDREW CHEN,[1] ARJUN VIRK,[1] ZACHERY HARRIS,[1] AZIN ABAZARI,[2] ROBERT HONKANEN,[2] AND M. HASSAN ARBAB[1,*]

[1]Department of Biomedical Engineering, Stony Brook University, 100 Nicolls Rd, Stony Brook, NY 11794, USA
[2]Department of Ophthalmology, Renaissance School of Medicine, 101 Nicolls Rd, Stony Brook, NY 11794, USA
*hassan.arbab@stonybrook.edu

**Abstract:** Elevated intraocular pressure (IOP) results in endothelial layer damage that can induce corneal hydration perturbations. We investigated the potential of terahertz spectroscopy in measuring the IOP levels through mapping corneal water content. We controlled the IOP levels in *ex vivo* rabbit and porcine eye samples while monitoring the change in corneal hydration using a terahertz time-domain spectroscopy (THz-TDS) scanner. Our results showed a statistically significant increase in the THz reflectivity between 0.4 and 0.6 THz corresponding to the increase in the IOP. Endothelial layer damage was confirmed using scanning electron microscopy (SEM) of the corneal biopsy samples. Our empirical results indicate that the THz-TDS can be used to track IOP levels through the changes in corneal hydration.



## 1. Introduction

Open Angle Glaucoma (OAG) is one of the leading causes of irreversible blindness [1]. Vision loss is the result of elevated intraocular pressure (IOP) damaging the optic nerve over time. Early diagnosis of glaucoma is critical to manage elevated IOP and prevent the disease progression. Standard diagnostic markers include both elevated IOP and retinal nerve fiber layer damage [2]. However, the nerve damage is clinically detectable only after 40% of the retinal ganglion cells are lost [3]. An alternative approach would be to probe disease progression by assessing corneal endothelial layer health. Sustained IOP elevations are associated with decreased endothelial cell density [4,5]. Endothelial cells maintain normal corneal tissue hydration by the active transport of excess aqueous humor [6]. High corneal tissue water content (CTWC) leads to opacification as the stroma swells from the influx of fluid. Without treatment and regulatory action, corneal tissue would continuously imbibe fluid [7]. Therefore, changes in the CTWC can be used to discern the endothelial layer's health and function. However, direct and non-contact *in vivo* evaluation of the CTWC remains a challenge. Clinically, corneal hydration is estimated based on its correlation with the central corneal thickness (CCT) measurements. A linear regression using simultaneous weight and pachymetry measurements by Ytteborg *et al.* in 1965 is used to derive CTWC from CCT [8]. Recent *in vivo* studies have suggested that a linear relationship is valid for the normal (healthy) eyes, but the relationship becomes nonlinear in diseased conditions [9]. This problem has motivated the development of alternative corneal hydration sensing techniques. For example, brillouin microscopy uses near infrared light to probe the corneal tissue biomechanics to gauge CTWC *in vivo* [10,11]. Raman spectroscopy technique can directly assess CTWC using spectroscopic information but requires high fluence power or long integration times, which hinders its *in vivo* application [12].

#423741 https://doi.org/10.1364/BOE.423741
Journal © 2021 Received 1 Mar 2021; revised 3 May 2021; accepted 4 May 2021; published 17 May 2021

Biomedical Optics EXPRESS

Terahertz (THz) spectroscopy has been gaining broader applications in the biomedical imaging field as a noninvasive, nondestructive, and sensitive tool for assessing tissue hydration or water content. As a measure of its high sensitivity, the noise equivalent delta water concentration (NEΔWC) of THz reflectivity to a polypropylene paper sample saturated to different hydration levels was calculated to be 0.054% [13]. Different groups have used terahertz time-domain spectroscopy (THz-TDS) to classify tissues in various disease models [14–18]. Grootentdorst *et al.* developed a handheld THz pulsed imaging scanner to differentiate *ex vivo* breast carcinoma tissue in freshly excised samples by its tissue water content [19,20]. Recently, *in vivo* THz-TDS measurements were used to grade wound severity in rodents [21] and porcine [22] burn models using hyperspectral parameters to assess tissue hydration and scattering in the skin [23].

In contrast, the homogenous nature of the corneal stroma layer, compared to other tissue types, makes it an apt target for hydration sensing using THz waves [24]. While the stroma of a healthy cornea presents as a homogeneous target in a plane perpendicular to the direction of propagation of the THz beam, its water content varies in the axial direction [25]. Early work by Bennett *et al.* demonstrated sensitivity of THz reflectivity to water content in *ex vivo* porcine corneal tissue [26]. Subsequent *ex vivo* studies have extracted the dielectric response of corneal tissue to variable hydration levels [27,28]. Recently, we have demonstrated a finite-difference time-domain model to solve the Fick's second law of diffusion in conjunction with the stratified Bruggeman model to predict, and experimentally verify, the change in the THz dielectric properties of a dehydrating corneal tissue phantom [29].

Several groups have demonstrated the clinical utility of THz reflectometry of corneal tissue using *in vivo* studies. Seminal work by Taylor *et al*. showed an increase in reflectivity at 100 GHz in rabbit eyes in contact with a mylar window corresponding to an increase in the CCT as the tissue rehydrates [9,24]. Ensuing systems utilized off-axis parabolic mirrors (OAPM) for non-contact imaging in humans [30,31]. A recent work explored the use of axicon lenses, designed for operation between 0.220 to 0.330 THz, for improved illumination of the cornea [32,33]. Other *in vivo* work has explored the potential of monitoring tear film thickness [28,34,35] and monitoring scleral and corneal hydration using THz waves between 130 and 320 GHz [36].

In this paper, we present experimental THz-TDS results obtained in two *ex vivo* studies using rabbit and porcine eyes, designed to observe CTWC changes due to elevated IOP levels. In both sets of experiments, the IOP was increased by raising the height of a saline reservoir connected to the anterior chamber of the samples [37–39]. Measurements of the rabbit samples in the first study were obtained using a collocated THz-TDS setup featuring telecentric beam steering and an f-θ lens to achieve a large field-of-view (FOV) with normal incidence angle [40], where corneal samples were in contact with a fused silica window. In the second study, porcine samples were measured in a non-contact THz-TDS corneal scanner utilizing an off-axis parabolic mirror (OAPM) to scan the spherical geometry of the eyeballs [30,31,41]. In both cases, the THz reflectivity increased as the IOP increased beyond the normal range of approximately 15-20 mmHg. Moreover, the statistically significant signal contrast between the experimental and control measurements was achieved in the frequencies between 0.45 and 0.6 THz within the broadband spectral range of our corneal scanner. Endothelial layer damage was confirmed in porcine samples with scanning electron microscopy (SEM). Our results demonstrate the potential of using THz-TDS measurements for the early detection of elevated IOP by monitoring the pressure-induced endothelial damage.

## 2. Methods

### 2.1. Ex vivo rabbit corneal studies

In the first study, rabbit eyes were chosen for their similarity in corneal thickness and anterior chamber depth to that of humans [42]. Rabbit eye samples were harvested from euthanized animals at the conclusion of ongoing studies at the Stony Brook University's Division of

Biomedical Optics EXPRESS

Laboratory Animal Research (DLAR) and approved by the Institutional Animal Care and Use Committee (IACUC). After excision, all samples were maintained in normal saline at 4 degrees C and used within 72 hours upon receival in accordance with established protocols for *ex vivo* tissue viability [43]. Samples were secured in styrofoam holders with agar gel to limit movement. As shown in Fig. 1(a), a 30 gauge needle was inserted into the anterior chamber of the eye to connect to the saline reservoir. During the study, the height of the reservoir was raised relative to the sample's to increase the IOP levels. Additionally, as the control experiment, this pressure was measured directly by a pressure sensor, Validyne DP15 (Validyne Inc, Los Angeles, CA), connected via a second 30-gauge needle placed in the anterior chamber. The IOP values started at 10 mmHg and were increased in seven 10 mmHg steps every approximately 3.4 hours during the total 24-hour study duration. For reference, in humans with chronic glaucoma IOP is usually between 20 and 30 mmHg on average, while acute glaucoma is associated with pressures greater than 40 mmHg [44].

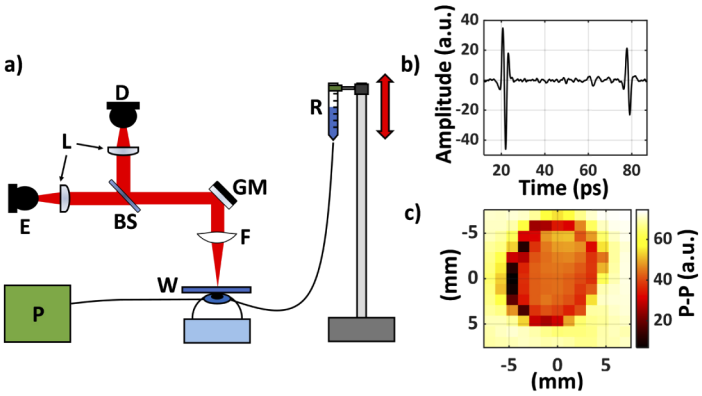


**Fig. 1.** (a) A schematic of the setup used in the first (rabbit) study. E, emitter; D, detector; W, fused silica imaging window; BS, silicon beam splitter; L, lenses (TPX50); GM, gimballed mirror; R, saline reservoir; P, Pressure sensor; F, f-θ lens; (b) A representative THz-TDS signal obtained from the center of the cornea through the imaging window is shown. There are two reflections; the first is from the air-fused silica interface and the second is from the fused silica-cornea interface. (c) A representative image of the corneal sample is formed using the peak-to-peak value of the second THz-TDS reflection pulse shown in (b).

As the IOP was increased, a series of THz-TDS scans were obtained using the first corneal scanner, shown in Fig. 1(a). The photoconductive antenna (PCA) emitter and detector were part of a commercial THz-TDS system, TeraSmart (Menlo System, Inc, Newton, NJ). TeraSmart uses a 1560 nm femtosecond fiber laser to pump an InGaAs/InAlAs PCA emitter, while a mechanical delay allows for the time-domain sampling of a LT InGaAs/InAlAs PCA detector with 0.0333 ps resolution. After the THz generation, the beam is collimated by a TPX50 lens (aspheric, 50 mm focal length, 38.1 mm diameter), passed through a silicon beam splitter and focused by an f-θ lens onto the fused silica window. A gimballed mirror placed in a telecentric configuration is used to steer the collimated beam across the f-θ lens and thus the imaging window to form a large FOV image. The f-θ lens maintains a fixed spot size throughout the scan [45]. The fused silica window is necessary due to the non-planar geometry of the eye samples. The returning beam is reflected by the beam splitter and focused by a second TPX 50 lens onto the detector.

A 13 by 13-pixel image with 1 $mm^2$ pixel area was obtained every 20 minutes over the course of a 24-hour experiment. As shown in Fig. 1(b), the THz signals were further processed using a high-pass gaussian filter to eliminate the internal low frequency (below 0.1 THz) intercoupling between the emitter and detector PCAs through the beam splitter. In Fig. 1(c), the peak-to-peak

Biomedical Optics EXPRESS

values (p-p) of the second reflection from the fused silica-cornea interface were calculated to form a representative image of the sample. The area of contact can be approximated as a circle with 5 mm radius. Based on the average rabbit corneal surface area approximately 50% of the cornea was in contact with the window [46]. Although the experimental setup described in this section provided for a rapid and easy investigation of any potential THz signal contrast mechanisms, it does suffer from the need to make direct contact between the spherical sample and the imaging window to ensure normal beam incidence. In the next section, we will use a new THz-TDS scanner for spherical samples using two linear motorized stages to achieve noncontact corneal imaging. Moreover, we will describe a time-domain approach for auto-alignment of the entire system in case of sample motion through addition of 3D positioning control for an OAPM used for mapping spherical surfaces.

### 2.2. *Ex vivo porcine corneal studies*

In the second study, porcine eyes were chosen due to their availability in large quantities and for their similarity in size to a human eyeball [47]. *Ex vivo* samples were obtained from a commercial vendor (First VisionTech, Inc, Sunnyvale, TX). Similar to the first study, the globes were secured in styrofoam holders using agar gel. The IOP levels were controlled using the height of the saline reservoir. In this study, the samples were divided between two groups: control (sham) and elevated-IOP (experimental) arms. In the experimental samples group (N = 4), the IOP values began at 15 mmHg and increased in steps of 10 mmHg every hour until reaching 55 mmHg. Control samples (N = 3) were maintained at a physiologically normal 15 mmHg for the same experimental duration [48]. The initial and ending central corneal thickness (CCT) were measured using an ultrasound pachymetry unit (Pachette 2, DGH Technologies, Exton, PA, USA). As shown in Fig. 2(a), the pressure sensor was connected via a 3-way stopcock to reduce the number of needles inserted in the anterior chamber as compared to the first study.

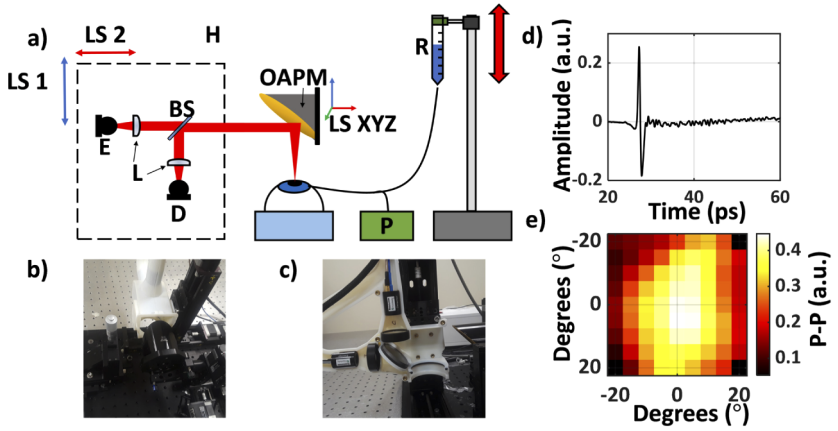


**Fig. 2.** (a) A schematic of the setup used in the second (porcine) study. E, emitter; D, detector; BS, silicon beam splitter; R, saline reservoir; P, Pressure sensor; OAPM, off-axis parabolic mirror; H, 3D-printed housing unit containing the imaging optics, mounted on the LS1 and LS2, linear stage motors, used to move the housing; LS XYZ, a 3-axis linear motorized stage used for 3D positioning and adjustments of the OAPM; (b) An image of the entire system. (c) Photograph of the 3D-printed housing mounted on its accompanying linear stages (LS1 and LS2). (d) A representative THz-TDS signal from the center of the image. (e) An equiangular raster scan image of the corneal sample formed using the p-p of the reflected THz pulse.

Biomedical Optics EXPRESS

A non-contact THz corneal scanner designed for ultimate clinical applications was tested in the second *ex vivo* study in this paper. To draw a parallel, contactless tonometers are predominantly preferred over contact tonometers due to ease of training, lack of local anesthesia requirement, low possibility of corneal infection or abrasion and objective measurements [49–52]. Based on previous work by Sung *et al*. [30,31,53,54], a 90-degree OAPM (EFL = 50.8 mm; Diameter = 76.2 mm) replaced the f-θ lens for focusing the THz beam onto the ocular globe. An OAPM with a sufficiently large aperture can focus collimated beams without spherical aberrations. A collimated beam raster scanning the aperture of an oversized OAPM at normal incidence angle is focused perpendicularly on the spherical target surface, whose center of curvature coincides with the focal point of the OAPM. Therefore, a grid of rectilinear coordinates on the OAPM's aperture surface can be mapped to a grid of angular coordinates on the spherical target surface. The spatial resolution of the scanner for imaging the spherical surface of the eye is estimated to be 1 mm. Further detail on the integration of the corneal scanner with a THz-TDS instrument, scanning coordinate mapping, and spherical spatial and axial resolution limits are described in our earlier publication [41]. The center of a spherical target is aligned to the focal point of the OAPM using strategies detailed in Virk *et al*. [41,55]. To maintain alignment during the scan, the emitter, detector and corresponding focusing optics are housed in a 3D-printed case and moved in unison. The collimated beam is raster scanned across the OAPM via two linear stage motors attached to the housing unit. A 9 by 9-pixel equiangular scan with 5° spacing was measured every 4 minutes. As it will be explained in the section below, an auto-alignment script repositions the OAPM between each scan, using three additional orthogonal linear stages controlling the OAPM's position, to ensure that the corneal hemisphere maintains proper scanning alignment with the OAPM. This auto-alignment process is critical to ensure accurate measurements are obtained because as the IOP increases, the corneal thickness increases and results in inflation of the sample surface. At the conclusion of the experiment, corneas were excised, fixed in 2.5% glutaraldehyde and 1.5% formaldehyde, dried using a series of ethanol and hexamethyldisilazane (HDMS) solutions and imaged with scanning electron microscopy (SEM) to confirm endothelial layer damage. The measured THz-TDS signals were high pass filtered with a gaussian filter to eliminate low frequency noise below 0.1 THz. A sample filtered THz-TDS signal is shown in Fig. 2(d), along with a representative image of the corneal sample in Fig. 2(e).

### 2.3. Auto-alignment of the porcine samples

In biomechanical studies of the cornea, tissue deformations due to increased IOP are used to gauge the sample's tensile properties [56,57]. To account for similar corneal deformations, an auto alignment script compensated for shifts in the apical position of the corneal hemisphere by slight adjustments to the OAPM's position. Because the path length is preserved for all beams incident to the OAPM, variations in the time of arrival (TOA) of the THz-TDS signals provide information on the sample's alignment. Prior to OAPM adjustments, as shown in Fig. 3, the TOAs of the central two axes of the target were recorded. The measured TOA values are converted to surface optical depth by Eq. (1),

$$Depth = c * \frac{(TOA - TOA_0)}{2} \tag{1}$$

where TOA is the time of arrival of each pixel and $TOA_0$ is defined as the time of arrival of the center pixel of the image, where the beam is focused on the apex of the spherical target, and c is the speed of light. Each cross scan, shown in Fig. 3(a), takes on average 15 seconds to complete. Based on calibration measurements using a metallic spherical reference, depth measurement resolution of the system is expected to be around 20 micrometers or less [40]. A sample misalignment, as shown in Fig. 3(a), creates a linear trend in the TOA of the pulses as a function of angular axis θ and φ. This information is used to iteratively adjust the 5 linear stages,

Biomedical Optics EXPRESS

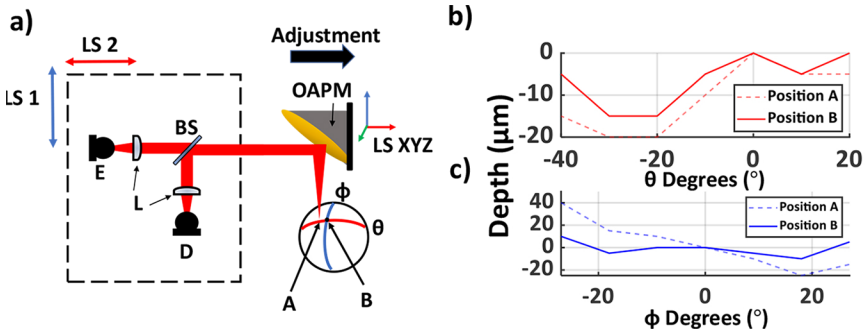


**Fig. 3.** (a) A schematic of the setup. E, emitter; D, detector; BS, silicon beam splitter; LS 1 and 2, Linear stage motors designated to move the emitter and detector in tandem for beam steering; LS XYZ, 3D linear stage motors controlling the OAPM's position. (b-c) Depth differences across the θ and φ axes at positions A and B, where position A is intentionally misaligned and B represents the properly aligned sample. The scanning range differs between the two axes due to the asymmetric nature of the OAPM's FOV.

which control the position of the THz-TDS housing and the OPAM accordingly until the depth range is below the aforementioned threshold. The emitter and detector housing unit are moved in tandem with the OAPM's position to retain the alignment of the system. Figure 3(b-c) show the surface optical depth measurements in an internationally misaligned sample (position A) and a well-aligned sample, designated by position B, along the θ and φ axes.

## 3. Results

### 3.1. Rabbit study

To assess the change in CTWC, we monitored the change in the peak-to-peak (p-p) amplitude of the THz-TDS reflection from the fused silica window-cornea interface. A total of three *ex vivo* rabbit samples were used in the first study. The central nine pixels of each scan were averaged as displayed in Fig. 4(a). Prior to averaging, experimental measurements were normalized using Eq. (2),

$$\%THz - TDS\ Amplitude = \frac{x_i - x_{min}}{x_{min}} * 100 \tag{2}$$

where $x_i$ is the THz p-p time series of each pixel and $x_{min}$ refers to the minimum THz amplitude value of each pixel. The results show an increase in the THz reflectivity. Figure 4(b) shows the averaged percentage increase in the THz amplitude of the central nine pixels of each of the samples with error bars representing the standard deviations of the experiments.

### 3.2. Porcine study

Figure 5 compares the mean change in the THz time-domain p-p amplitude of the averaged central nine pixels of each corneal image, represented in Fig. 5(a) by the rectangular ROI, for both the control and experimental groups.

The percentage change in the normalized THz-TDS amplitudes was calculated using Eq. (2). A moving average filter of length 5 was applied to the mean THz amplitude change time series. Our results in Fig. 5(b) shows that the increase in the mean THz amplitude was statistically significant after 35 mmHg, as compared to the control group. A Student's t-test was used at each time point to calculate statistical significance between the control and experimental samples. An asterisk represents a significant difference with a *p*-value less than 0.05.

Biomedical Optics EXPRESS

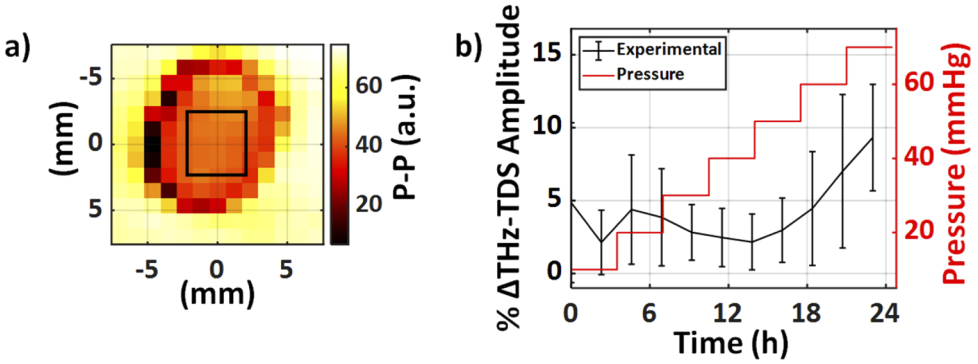


**Fig. 4.** (a) The THz-TDS amplitude of the central 9 pixels, shown by the rectangular ROI, were used in the calculation. (b) The normalized percentage increase in the THz amplitude of the reflection from the fused silica window-cornea interface is plotted with error bars representing ± the standard deviation of the experiments.

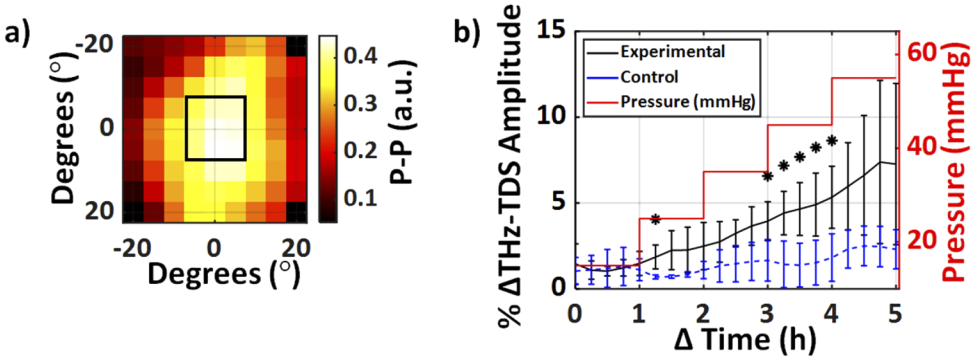


**Fig. 5.** (a) A representative corneal THz-TDS amplitude image obtained using the non-contact spherical scanner displaying the central nine pixels as the ROI in each sample. (b) The mean normalized change in the averaged THz-TDS amplitude of the ROI is plotted over time between the experimental and control samples. The red trace shows the measured stepwise IOP in the experimental group, while this value was kept constant at 15 mmHg for the control group (not shown). The error bars represent ± standard deviation. Asterisks represent a statistically significant difference at that time point ($p < 0.05$).

Biomedical Optics EXPRESS

Results shown in Fig. 5 were calculated using the time-domain p-p amplitudes of the THz pulses. To determine the frequency dependence of the observed signal contrast, the Fourier transform of the THz-TDS signals were calculated and deconvolved with a reference measurement obtained using a stainless-steel spherical target (r = 8.02 mm). The resulting spectra are shown in Fig. 6(a-b) for a representative experimental and control cornea, respectively. In Fig. 6, the time-dependence of the deconvolved THz spectra is plotted between 0.25 and 0.55 THz, showing a monotonic increase in THz reflectively in experimental samples as compared to the control group.

Fourier domain analysis of the THz scans obtained in this study showed that the area under the curve (AUC) of the spectral amplitude between 0.45 and 0.6 THz provided the largest statistical significance, as shown in Fig. 7.

To confirm endothelial damage, SEM images of the porcine samples were obtained at the conclusion of the experiments. In Fig. 8(a), the control samples have the regular characteristic hexagonal arrangement of the healthy endothelial cells in the control group. In contrast, the

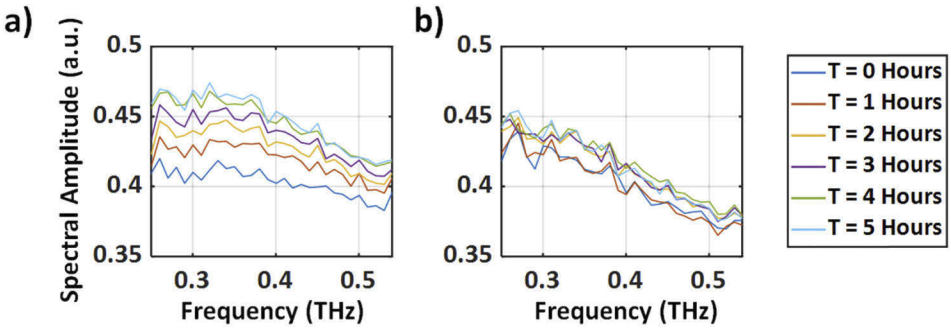


**Fig. 6.** (a) A representative deconvolved THz spectrum of the experimental group throughout the 5-hour duration as the IOP was increased. (b) A representative deconvolved THz spectrum of the control group over the 5-hour window while the IOP was kept constant at 15 mmHg.

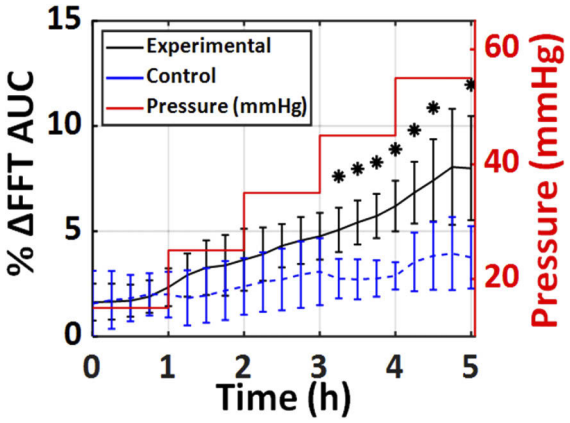


**Fig. 7.** The mean percentage change in the AUC of the THz spectra, between 0.45 and 0.6 THz, in both the experimental and control groups is plotted. The red step profile shows the IOP of the experimental group over the 5 hours. In contrast, the IOP of the control group was held constant at 15 mmHg (not shown). The error bars represent ± standard deviation. The asterisks represent a significant difference between the experimental and control group with $p < 0.05$.

Biomedical Optics EXPRESS

experimental samples in Fig. 8(b) show extensive damage to the corneal endothelial layer. The increase in tissue water content occurs due to the damage to the corneal endothelial layer caused by the increasing IOP. Increased water content results in a higher index of refraction, which in turn gives rise to higher reflectivity. We estimate that a change from 70% to 80% in CTWC results in an approximate 3.37% increase in the real part of the index of refraction at 0.5 THz (the center frequency of the THz-TDS system). Finally, Fig. 8(c) shows the result from the pachymetry readings before and after each experiment. Here, the increase in the CCT in the experimental group is due to the influx of fluid after the elevated IOP damaged the endothelial layer barrier. In the control group, however, due to the lower sustained IOP the endothelium is intact, and consequently the excess fluid imbibed in the sample during the storage is squeezed out after acclimatization to normal IOP levels [56]. Therefore, while the CCT has increased in the experimental arm over the course of the 5 hours, it has decreased in the control group.

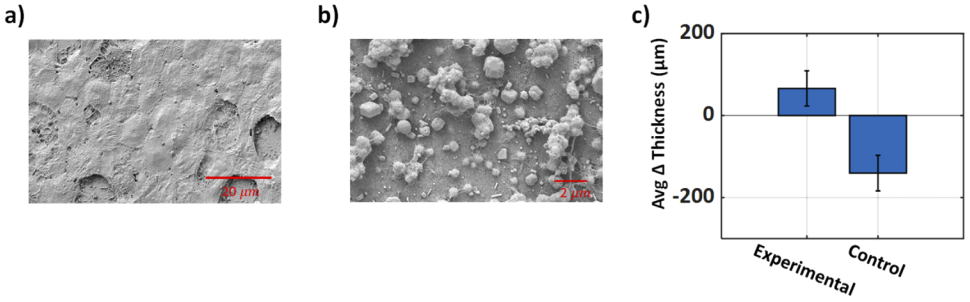


**Fig. 8.** (a) Representative SEM image of the endothelial layer of a porcine cornea where the IOP was maintained at 15 mmHg. (b) Representative SEM image of a porcine cornea in the experimental group. The biopsy was collected after the IOP was increased to 55 mmHg. (c) The mean change in CCT measured using ultrasound pachymetry before and after each experiment are plotted in both groups. The error bars represent the standard deviation of thickness measurements.

## 4. Conclusions

By increasing IOP using a variable height saline reservoir in two *ex vivo* studies, we tested the hypothesis that the THz spectral reflectivity of the cornea is higher in eyeballs suffering from elevated IOP levels as compared to normal eyes due to an increased CTWC. We reported *ex vivo* measurement results using two THz-TDS systems featuring a wide FOV, using an f-θ lens (contact based) and an OAPM (non-contact) developed for scanning spherical surfaces. An auto alignment script was necessary to ensure the apex of the corneal surface remained aligned to the OAPM as the IOP was increased. Despite differences in species of *ex vivo* samples and the THz-TDS setups used, we have demonstrated that the THz-TDS spectroscopy can monitor pressure-driven CTWC changes. Spectral intensities between 0.45 and 0.6 THz were shown to be a more discerning marker of CTWC changes in comparison to THz-TDS pulse amplitude in the time-domain. Finally, we proposed a potential pathway for the increased CTWC due to observed damage to the endothelial tight junctions in the experimental corneas. Future work includes improving the clinical applicability of the THz-TDS corneal scanner by increasing measurement speed. While satisfactory for *ex vivo* samples, the several-minute-long scan times would not be robust to motion artifacts expected during *in vivo* measurements. One potential solution may involve incorporating broadband compressed sensing to decrease scan times, while retaining spectral information [58].

**Funding.** Stony Brook University; National Institute of General Medical Sciences (R01GM112693).

Biomedical Optics EXPRESS

**Acknowledgements.** The authors would like to thank the Department of Laboratory Animal Resources and specifically the veterinary staff for providing us advice and samples.

**Disclosures.** The authors declare that there are no conflicts of interest related to this work.

**Data availability.** Data underlying the results presented in this paper are not publicly available at this time but may be obtained from the authors upon reasonable request.

## References

1. J. K. S. Parihar, "Glaucoma: The "Black hole" of irreversible blindness," Med. J. Armed Forces India **72**(1), 3–4 (2016).
2. F. A. Medeiros, L. M. Alencar, L. M. Zangwill, P. A. Sample, and R. N. Weinreb, "The Relationship between intraocular pressure and progressive retinal nerve fiber layer loss in glaucoma," Ophthalmology **116**(6), 1125–1133.e3 (2009).
3. M. P. Y. Chan, D. C. Broadway, A. P. Khawaja, J. L. Y. Yip, D. F. Garway-Heath, J. M. Burr, R. Luben, S. Hayat, N. Dalzell, K.-T. Khaw, and P. J. Foster, "Glaucoma and intraocular pressure in EPIC-Norfolk Eye Study: cross sectional study," BMJ **358**, j3889 (2017).
4. M.-M. Gagnon, H. M. Boisjoly, I. Brunette, M. Charest, and M. Amyot, "Corneal endothelial cell density in glaucoma," Cornea **16**(3), 314–318 (1997).
5. Z.-Y. Yu, L. Wu, and B. Qu, "Changes in corneal endothelial cell density in patients with primary open-angle glaucoma," WJCC **7**(15), 1978–1985 (2019).
6. S. Feizi, "Corneal endothelial cell dysfunction: etiologies and management," Ther. Adv. Ophthalmol. **10**, 251584141881580 (2018).
7. X. Cheng, S. J. Petsche, and P. M. Pinsky, "A structural model for the in vivo human cornea including collagen-swelling interaction," J. R. Soc., Interface **12**(109), 20150241 (2015).
8. J. Ytteborg and C. H. Dohlman, "Corneal edema and intraocular pressure: II. Clinical results," Arch. Ophthalmol. **74**(4), 477–484 (1965).
9. Z. D. Taylor, J. Garritano, S. Sung, N. Bajwa, D. B. Bennett, B. Nowroozi, P. Tewari, J. W. Sayre, J.-P. Hubschman, S. X. Deng, E. R. Brown, and W. S. Grundfest, "THz and mm-wave sensing of corneal tissue water content: in vivo sensing and imaging results," IEEE Trans. Terahertz Sci. Technol. **5**(2), 184–196 (2015).
10. P. Shao, T. G. Seiler, A. M. Eltony, A. Ramier, S. J. J. Kwok, G. Scarcelli, R. P. Ii, and S.-H. Yun, "Effects of corneal hydration on brillouin microscopy in vivo," Invest. Ophthalmol. Visual Sci. **59**(7), 3020–3027 (2018).
11. T. G. Seiler, P. Shao, B. E. Frueh, S.-H. Yun, and T. Seiler, "The influence of hydration on different mechanical moduli of the cornea," Graefe's Arch. Clin. Exp. Ophthalmol. **256**(9), 1653–1660 (2018).
12. D. A. Ammar, T. C. Lei, M. Y. Kahook, and O. Masihzadeh, "Imaging the intact mouse cornea using coherent anti-Stokes Raman scattering (CARS)," Invest. Ophthalmol. Visual Sci. **54**(8), 5258–5265 (2013).
13. Z. Taylor, R. Singh, M. Culjat, J. Suen, W. Grundfest, and E. Brown, "THz imaging based on water-concentration contrast," Proc. SPIE **6949**, 69490D (2008).
14. H. Lindley-Hatcher, A. I. Hernandez-Serrano, J. Wang, J. Cebrian, J. Hardwicke, and E. Pickwell-MacPherson, "Evaluation of in vivo THz sensing for assessing human skin hydration," JPhys Photonics **3**(1), 014001 (2020).
15. Q. Sun, E. P. J. Parrott, Y. He, and E. Pickwell-MacPherson, "In vivo THz imaging of human skin: Accounting for occlusion effects," J. Biophotonics **11**(2), e201700111 (2018).
16. Y. Zou, J. Li, Y. Cui, P. Tang, L. Du, T. Chen, K. Meng, Q. Liu, H. Feng, J. Zhao, M. Chen, and L.-G. Zhu, "Terahertz spectroscopic diagnosis of myelin deficit brain in mice and rhesus monkey with chemometric techniques," Sci. Rep. **7**(1), 5176 (2017).
17. S. Yamaguchi, Y. Fukushi, O. Kubota, T. Itsuji, T. Ouchi, and S. Yamamoto, "Brain tumor imaging of rat fresh tissue using terahertz spectroscopy," Sci. Rep. **6**(1), 30124 (2016).
18. M. El-Shenawee, N. Vohra, T. Bowman, and K. Bailey, "Cancer detection in excised breast tumors using terahertz imaging and spectroscopy," Biomed. Spectrosc. Imaging **8**(1-2), 1–9 (2019).
19. M. R. Grootendorst, A. J. Fitzgerald, S. G. B. de Koning, A. Santaolalla, A. Portieri, M. Van Hemelrijck, M. R. Young, J. Owen, M. Cariati, M. Pepper, V. P. Wallace, S. E. Pinder, and A. Purushotham, "Use of a handheld terahertz pulsed imaging device to differentiate benign and malignant breast tissue," Biomed. Opt. Express **8**(6), 2932–2945 (2017).
20. A. J. Fitzgerald, V. P. Wallace, M. Jimenez-Linan, L. Bobrow, R. J. Pye, A. D. Purushotham, and D. D. Arnone, "Terahertz pulsed imaging of human breast tumors," Radiology **239**(2), 533–540 (2006).
21. M. H. Arbab, D. P. Winebrenner, T. C. Dickey, M. B. Klein, A. Chen, and P. D. Mourad, "A noninvasive terahertz assessment of 2nd and 3rd degree burn wounds," in *Conference on Lasers and Electro-Optics 2012, OSA Technical Digest (Online)* (Optical Society of America, 2012), p. CTu3B.3.
22. O. B. Osman, T. Jack Tan, S. Henry, A. Warsen, N. Farr, A. M. McClintic, Y.-N. Wang, S. Arbabi, and M. H. Arbab, "Differentiation of burn wounds in an in vivo porcine model using terahertz spectroscopy," Biomed. Opt. Express **11**(11), 6528–6535 (2020).
23. Omar Osman, Zachery Harris, Juin Zhou, Mahmoud Khani, Adam Singer, and M. Arbab, Res. Sq. (2021).
24. Z. D. Taylor, R. S. Singh, D. B. Bennett, P. Tewari, C. P. Kealey, N. Bajwa, M. O. Culjat, A. Stojadinovic, H. Lee, J.-P. Hubschman, E. R. Brown, and W. S. Grundfest, "THz medical imaging: in vivo hydration sensing," IEEE Trans. Terahertz Sci. Technol. **1**(1), 201–219 (2011).

Biomedical Optics EXPRESS


25. Z. D. Taylor, J. Garritano, S. Sung, N. Bajwa, D. B. Bennett, B. Nowroozi, P. Tewari, J. Sayre, J.-P. Hubschman, S. Deng, E. R. Brown, and W. S. Grundfest, "THz and mm-wave sensing of corneal tissue water content: electromagnetic modeling and analysis," IEEE Trans. Terahertz Sci. Technol. **5**(2), 170–183 (2015).
26. D. B. Bennett, Z. D. Taylor, P. Tewari, R. S. Singh, M. O. Culjat, W. S. Grundfest, D. J. Sassoon, R. D. Johnson, J.-P. Hubschman, and E. R. Brown, "Terahertz sensing in corneal tissues," J. Biomed. Opt. **16**(5), 057003 (2011).
27. M. Mizuno, H. Kitahara, K. Sasaki, M. Tani, M. Kojima, Y. Suzuki, T. Tasaki, Y. Tatematsu, M. Fukunari, and K. Wake, "Dielectric property measurements of corneal tissues for computational dosimetry of the eye in terahertz band in vivo and in vitro," Biomed. Opt. Express **12**(3), 1295–1307 (2021).
28. O. A. Smolyanskaya, N. V. Chernomyrdin, A. A. Konovko, K. I. Zaytsev, I. A. Ozheredov, O. P. Cherkasova, M. M. Nazarov, J.-P. Guillet, S. A. Kozlov, Yu. V. Kistenev, J.-L. Coutaz, P. Mounaix, V. L. Vaks, J.-H. Son, H. Cheon, V. P. Wallace, Yu. Feldman, I. Popov, A. N. Yaroslavsky, A. P. Shkurinov, and V. V. Tuchin, "Terahertz biophotonics as a tool for studies of dielectric and spectral properties of biological tissues and liquids," Prog. Quantum Electron. **62**, 1–77 (2018).
29. A. Chen, O. B. Osman, Z. B. Harris, A. Abazri, R. Honkanen, and M. H. Arbab, "Investigation of water diffusion dynamics in corneal phantoms using terahertz time-domain spectroscopy," Biomed. Opt. Express **11**(3), 1284–1297 (2020).
30. S. Sung, S. Selvin, N. Bajwa, S. Chantra, B. Nowroozi, J. Garritano, J. Goell, A. Li, S. X. Deng, E. Brown, W. S. Grundfest, and Z. D. Taylor, "THz imaging system for in vivo human cornea," IEEE Trans. Terahertz Sci. Technol. **8**(1), 27–37 (2018).
31. S. Sung, S. Dabironezare, N. Llombart, S. Selvin, N. Bajwa, S. Chantra, B. Nowroozi, J. Garritano, J. Goell, A. Li, S. X. Deng, E. Brown, W. S. Grundfest, and Z. D. Taylor, "Optical system design for noncontact, normal incidence, THz imaging of in vivo human cornea," IEEE Trans. Terahertz Sci. Technol. **8**(1), 1–12 (2018).
32. A. Tamminen, S. Pälli, J. Ala-Laurinaho, M. Salkola, A. V. Räisänen, and Z. Taylor, "Axicon-hyperbolic lens for reflectivity measurements of curved surfaces," in *2020 14th European Conference on Antennas and Propagation (EuCAP)* (2020), pp. 1–5.
33. A. Tamminen, S.-V. Palli, J. Ala-laurinaho, M. Salkola, A. Raisanen, and Z. Taylor, "Quasioptics for corneal sensing at 220 - 330 GHz: design, evaluation, and ex-vivo cornea parameter extraction," IEEE Trans. Terahertz Sci. Technol., 1 (2020).
34. I. Ozheredov, M. Prokopchuk, M. Mischenko, T. Safonova, P. Solyankin, A. Larichev, A. Angeluts, A. Balakin, and A. Shkurinov, "In vivoTHz sensing of the cornea of the eye," Laser Phys. Lett. **15**(5), 055601 (2018).
35. I. Ozheredov, T. Safonova, E. Sikach, M. Mischenko, M. Prokopchuk, A. Larichev, Y. Listopadskaya, and A. Shkurinov, "Potential clinical applications of terahertz reflectometry for the assessment of the tear film stability," Opt. Eng. **59**(06), 1–7 (2020).
36. E. N. Iomdina, G. N. Goltsman, S. V. Seliverstov, A. A. Sianosyan, K. O. Teplyakova, and A. A. Rusova, "Study of transmittance and reflectance spectra of the cornea and the sclera in the THz frequency range," J. Biomed. Opt. **21**(9), 097002 (2016).
37. M. Stockslager, B. Samuels, R. R. Allingham, Z. Klesmith, S. Schwaner, C. Forest, and C. Ethier, "System for rapid, precise modulation of intraocular pressure, toward minimally-invasive in vivo measurement of intracranial pressure," PLoS One **11**(1), e0147020 (2016).
38. J. Lim, S. Kang, S. Park, E. Park, T. Nam, S. Jeong, and K. Seo, "Intraocular pressure measurement by rebound tonometry (tonovet) in normal pigeons (columba livia)," J. Avian Med. Surg. **33**(1), 46–52 (2019).
39. L. He, M. Wendt, and A. Glasser, "Manipulation of intraocular pressure for studying the effects on accommodation," Exp. Eye Res. **102**, 76–84 (2012).
40. Z. B. Harris, A. Virk, M. E. Khani, and M. H. Arbab, "Terahertz time-domain spectral imaging using telecentric beam steering and an f-θ scanning lens: distortion compensation and determination of resolution limits," Opt. Express **28**(18), 26612–26622 (2020).
41. A. S. Virk, Z. B. Harris, and M. H. Arbab, "Development of a terahertz time-domain scanner for topographic imaging of spherical targets," Opt. Lett. **46**(5), 1065–1068 (2021).
42. E. Zernii, V. Baksheeva, E. Iomdina, O. Averina, S. Permyakov, P. Philippov, A. Zamyatnin, and I. Senin, "Rabbit models of ocular diseases: new relevance for classical approaches," CNS Neurol. Disord.: Drug Targets **15**(3), 267–291 (2016).
43. A. Wilson, J. Jones, J. R. Tyrer, and J. Marshall, "An interferometric ex vivo study of corneal biomechanics under physiologically representative loading, highlighting the role of the limbus in pressure compensation," Eye Vis. **7**(1), 43 (2020).
44. P. T. Khaw, P. Shah, and A. R. Elkington, "Glaucoma–1: diagnosis," BMJ **328**(7431), 97–99 (2004).
45. Z. B. Harris, S. Katletz, M. E. Khani, A. Virk, and M. H. Arbab, "Design and characterization of telecentric f-θ scanning lenses for broadband terahertz frequency systems," AIP Adv. **10**(12), 125313 (2020).
46. M. A. Watsky, M. M. Jablonski, and H. F. Edelhauser, "Comparison of conjunctival and corneal surface areas in rabbit and human," Curr. Eye Res. **7**(5), 483–486 (1988).
47. I. Sánchez, R. Martin, F. Ussa, and I. Fernandez-Bueno, "The parameters of the porcine eyeball," Graefe's Arch. Clin. Exp. Ophthalmol. Albrecht Von Graefes Arch. Für Klin. Exp. Ophthalmol. **249**(4), 475–482 (2011).
48. J. Ruiz-Ederra, M. García, M. Hernandez, H. Urcola, E. Hernández-Barbáchano, J. Araiz, and E. Vecino, "The pig eye as a novel model of glaucoma. Exp Eye Res 81(5):561-569," Exp. Eye Res. **81**(5), 561–569 (2005).
49. R. R. Allingham, S. Moroi, M. B. Shields, and K. Damji, *Shields' Textbook of Glaucoma* (Lippincott Williams & Wilkins, 2020).

Biomedical Optics EXPRESS


50. Q. K. Farhood, "Comparative evaluation of intraocular pressure with an air-puff tonometer versus a Goldmann applanation tonometer," Clin. Ophthalmol. **7**, 23–27 (2012).
51. J. M. Martinez-de-la-Casa, M. Jimenez-Santos, F. Saenz-Frances, M. Matilla-Rodero, C. Mendez-Hernandez, R. Herrero-Vanrell, and J. Garcia-Feijoo, "Performance of the rebound, noncontact and Goldmann applanation tonometers in routine clinical practice," Acta Ophthalmol. **89**(7), 676–680 (2011).
52. I. Yilmaz, C. Altan, E. D. Aygit, C. Alagoz, O. Baz, S. Ahmet, S. Urvasizoglu, D. Yasa, and A. Demirok, "Comparison of three methods of tonometry in normal subjects: Goldmann applanation tonometer, non-contact airpuff tonometer, and Tono-Pen XL," Clin. Ophthalmol. **8**, 1069–1074 (2014).
53. S. Sung, J. Garritano, N. Bajwa, S. Deng, J.-P. Hubschman, W. S. Grundfest, and Z. D. Taylor, "Preliminary results of non-contact THz imaging of cornea," Proc. SPIE **9362**, 93620C (2015).
54. S. Sung, S. Chantra, N. Bajwa, R. Mccurdy, G. Kerezyte, J. Garritano, J.-P. Hubschman, W. Grundfest, S. X. Deng, and Z. Taylor, "Direct measurement of corneal tissue water content by reflection imaging at Terahertz Frequencies," Invest. Ophthalmol. Visual Sci. **56**(7), 1644 (2015).
55. A. Virk, Z. B. Harris, and M. H. Arbab, "Development of a THZ-TDS scanner for topographic corneal imaging," in *2019 44th International Conference on Infrared, Millimeter, and Terahertz Waves (IRMMW-THz)* (2019), pp. 1–2.
56. A. Kazaili, S. Lawman, B. Geraghty, A. Eliasy, Y. Zheng, Y. Shen, and R. Akhtar, "Line-field optical coherence tomography as a tool for In vitro characterization of corneal biomechanics under physiological pressures," Sci. Rep. **9**(1), 6321 (2019).
57. L.-K. Wang, L. Tian, Y. Huang, Y. Huang, and Y. Zheng, "Assessment of corneal biomechanical properties with inflation test using optical coherence tomography," Ann. Biomed. Eng. **46**, 247–256 (2018).
58. R. I. Stantchev, X. Yu, T. Blu, and E. Pickwell-MacPherson, "Real-time terahertz imaging with a single-pixel detector," Nat. Commun. **11**(1), 2535 (2020).